

# First-principles calculation of lattice thermal conductivities of $\alpha$ -, $\beta$ -, and $\gamma$ - $\text{Si}_3\text{N}_4$

Kazuyoshi Tatsumi,<sup>1,2,\*</sup> Atsushi Togo,<sup>2</sup> and Isao Tanaka<sup>2,3,4</sup>

<sup>1</sup>*Institute of Materials and Systems for Sustainability,  
Nagoya University, Chikusa, Nagoya 464-8603, Japan*

<sup>2</sup>*Center for Elements Strategy Initiative for Structural Materials,  
Kyoto University, Sakyo, Kyoto 606-8501, Japan*

<sup>3</sup>*Department of Materials Science and Engineering,  
Kyoto University, Sakyo, Kyoto 606-8501, Japan*

<sup>4</sup>*Nanostructures Research Laboratory, Japan Fine Ceramics Center, Atsuta, Nagoya 456-8587, Japan*

The lattice thermal conductivities of  $\alpha$ -,  $\beta$ - and  $\gamma$ - $\text{Si}_3\text{N}_4$  phases are investigated from *ab-initio* anharmonic lattice dynamics, within the single-mode relaxation-time approximation of the linearized phonon Boltzmann transport equation. At 300 K, the lattice thermal conductivity of  $\beta$ - $\text{Si}_3\text{N}_4$  is calculated as  $\kappa_{xx} = 73$  and  $\kappa_{zz} = 199$  (in units of  $\text{W m}^{-1} \text{K}^{-1}$ ), which is consistent with the reported experimental values of 69 and 180, respectively. For  $\alpha$ - $\text{Si}_3\text{N}_4$ ,  $\kappa_{xx} = 68$  and  $\kappa_{zz} = 100$  are obtained. The difference in anisotropy between these phases originates from the characteristic differences in their phonon band structures, which is closely related to the crystal structures. In  $\alpha$ - $\text{Si}_3\text{N}_4$ , acoustic-mode phonons below 6 THz are the main heat carriers, while in  $\beta$ - $\text{Si}_3\text{N}_4$ , the phonon modes up to 12 THz contribute to the lattice thermal conductivity. In  $\gamma$ - $\text{Si}_3\text{N}_4$ ,  $\kappa = 77$  is obtained. The distribution of phonon mode contributions to the lattice thermal conductivity with respect to phonon frequency closely resembles that for  $\kappa_{xx}$  of  $\beta$ - $\text{Si}_3\text{N}_4$ , although the phonon lifetimes for  $\gamma$ - $\text{Si}_3\text{N}_4$  are twice as short as those for  $\beta$ - $\text{Si}_3\text{N}_4$ .

## I. INTRODUCTION

Several nitride insulators are known to exhibit high thermal conductivity, which is important for heat transfer materials at elevated temperatures. For example, Slack *et al.*<sup>1</sup> reported that wurtzite-type AlN has thermal conductivity that exceeds  $100 \text{ W m}^{-1} \text{K}^{-1}$ .  $\text{Si}_3\text{N}_4$  has become another promising thermal conductive insulator because its thermal conductivity has been improved up to  $177 \text{ W m}^{-1} \text{K}^{-1}$  through the use of advanced ceramic technologies related to densification and microstructure control.<sup>2-5</sup> The  $\text{Si}_3\text{N}_4$  ceramics also exhibit high mechanical strength at elevated temperatures; therefore, they are regarded as ideal materials for use in various applications, such as engine components, gas turbines, and heat sink substrates of power semiconductor devices.

At atmospheric pressure,  $\text{Si}_3\text{N}_4$  has two phases,  $\alpha$  and  $\beta$ , which are generally considered as low- and high-temperature phases, respectively.<sup>2,6,7</sup> Their crystal structures belong to the  $P31c$  and  $P6_3/m$  space groups, respectively.<sup>8,9</sup> These structures have different manners of stacking equivalent basal layer structures composed of  $\text{SiN}_4$  tetrahedra.<sup>10</sup> Fig. 1 depicts these layer structures from the principal axis direction. They are denoted as A, B, C, and D in the  $\alpha$  phase, and A and B in the  $\beta$  phase. The stacking manners are thus ABCDABCD... and ABAB..., respectively. The  $\alpha$  phase has additional two layer structures of C and D, which are related to A and B by the  $c$  glide operation.<sup>10</sup> Along this direction, the lattice constant of the  $\alpha$  phase is approximately twice as long as that of the  $\beta$  phase.

The experimental thermal conductivities<sup>2-5,12</sup> of the  $\text{Si}_3\text{N}_4$  polymorphs were measured for bulk polycrystalline samples. These values were significantly affected by the lattice defects, impurities, shapes and orientations of the

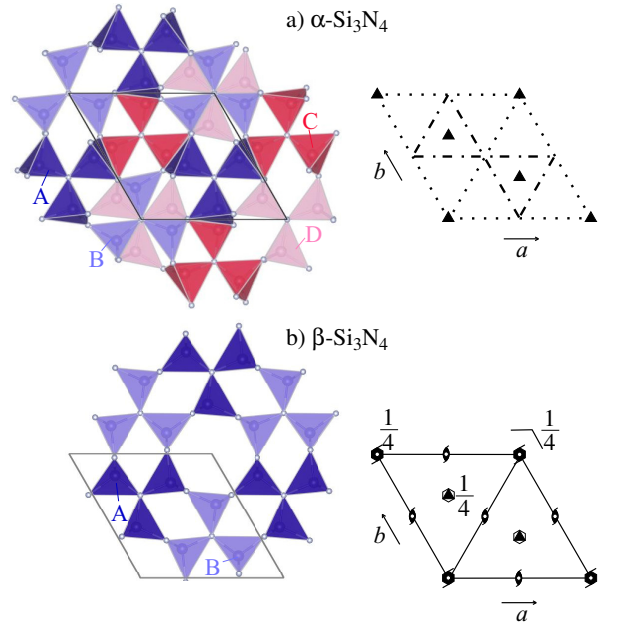


FIG. 1. (color online) Crystal structures of  $\alpha$ - and  $\beta$ - $\text{Si}_3\text{N}_4$ . Stacking of  $\text{SiN}_4$  tetrahedron layers are shown at the left. (a) ABCDABCD... for  $\alpha$ - $\text{Si}_3\text{N}_4$ . (b) ABAB... for  $\beta$ - $\text{Si}_3\text{N}_4$ . Space group diagrams<sup>11</sup> for  $P31c$  ( $\alpha$ - $\text{Si}_3\text{N}_4$ ) and  $P6_3/m$  ( $\beta$ - $\text{Si}_3\text{N}_4$ ) are shown at the right.

constituent crystal grains;<sup>6</sup> the intrinsic thermal conductivity of defect-free  $\text{Si}_3\text{N}_4$  has not been established. As an experimental approach to determine this, Li *et al.*<sup>13</sup> applied the high-resolution thermoreflectance microscopy to single  $\beta$ - $\text{Si}_3\text{N}_4$  grains in a ceramic sample. The thermal conductivity was analyzed as 69 and  $180 \text{ W m}^{-1} \text{K}^{-1}$  along the  $a$  and  $c$  axes, respectively. These val-

ues respectively correspond to the  $xx$  and  $zz$  elements of the lattice thermal conductivity tensor,  $\kappa$ . We consider the anisotropy of  $\kappa_{zz}/\kappa_{xx} \sim 3$  is relatively large. Hirotsaki *et al.*<sup>6</sup> theoretically estimated  $\kappa$  by application of the Green-Kubo formulation to the molecular dynamics (MD) method with the interatomic potentials proposed by Vashishta *et al.*<sup>14</sup>. They calculated  $\kappa_{xx}$  and  $\kappa_{zz}$  of  $\alpha$ -Si<sub>3</sub>N<sub>4</sub> to be 105 and 225 W m<sup>-1</sup> K<sup>-1</sup>, and those of  $\beta$ -Si<sub>3</sub>N<sub>4</sub> as 170 and 450 W m<sup>-1</sup> K<sup>-1</sup>, respectively. The ratio  $\kappa_{zz}/\kappa_{xx}$  in  $\beta$ -Si<sub>3</sub>N<sub>4</sub> agreed well with the experimental ratio;  $\kappa_{xx}$  and  $\kappa_{zz}$  were overestimated by more than two times those of the corresponding experimental  $\kappa$  values.

Based on first principles calculations and Boltzmann transport theory<sup>15</sup>, Togo *et al.* recently calculated  $\kappa$  of many polymorphs of the zincblende- and wurtzite-type structures. Their crystal structures have stacking manners of the densest atom planes as ABCABC... and ABAB..., respectively. The different stacking manners merely altered  $\kappa$ , the phonon linewidths and the phonon density of states (DOS).<sup>15</sup> On the other hand, the previous MD results indicated that the different stacking manners between the  $\alpha$  and  $\beta$  phases altered  $\kappa$  significantly. This has not been explained with respect to their phonon properties. Therefore, it is of interest to investigate this based on the first principles anharmonic phonon calculation.

In addition to the  $\alpha$  and  $\beta$  phases, a cubic spinel phase ( $\gamma$ -Si<sub>3</sub>N<sub>4</sub>) is known to form upon compression and *in situ* heating.<sup>16,17</sup> The reported transition pressures are scattered from 10 to 36 GPa, depending on the experimental conditions.<sup>18</sup> The  $\gamma$  phase is experimentally quenched to atmospheric pressure and room temperature. The thermal conductivity of the  $\gamma$  phase has not been experimentally reported, although it has been estimated by the Slack model.<sup>19</sup>

The present study aims to qualitatively elucidate the lattice thermal conductivity tensors among the three Si<sub>3</sub>N<sub>4</sub> phases by a first principles approach. We calculate  $\kappa$  of the  $\gamma$  phase as well, for systematic understanding. After the methodology is described, we examine the validity of the present results; through comparison of the calculated thermal properties with the available experimental and theoretical references.

The characteristic behaviors of  $\kappa$  are then investigated in detail on the basis of the phonon band structures and phonon linewidths.

## II. COMPUTATIONAL PROCEDURES

### A. Lattice thermal conductivity calculation

The lattice thermal conductivities were calculated by solving the linearized Boltzmann transport equation (LBTE) within the single-mode relaxation time approximation (single-mode RTA). The harmonic phonon states and lattice thermal conductivities were calculated with

the phonopy<sup>20</sup> and phono3py<sup>15</sup> software packages, respectively. We also attempted the direct-solution of LBTE<sup>21</sup> and give the calculated  $\kappa$  values in the following section. The difference between  $\kappa$  calculated by the single-mode RTA and that by the direct solution was minor for our discussion. Therefore, this research was limited to use the single-mode RTA to take advantage of the closed form of  $\kappa$ , which can be intuitively understood in terms of mode-specific phonon properties.

In the following sections, we denote the phonon mode by  $\lambda = (\mathbf{q}, p)$  with the set of the phonon wave vector  $\mathbf{q}$  and band index  $p$  and  $-\lambda \equiv (-\mathbf{q}, p)$ . The relaxation time due to phonon-phonon scattering was obtained as half the reciprocal of linewidth,  $\tau_{\lambda, \text{ph-ph}} = (2\Gamma_{\lambda})^{-1}$ , where the linewidth that was employed is as follows:

$$\Gamma_{\lambda} = \frac{18\pi}{\hbar^2} \sum_{\lambda'\lambda''} |\Phi_{-\lambda\lambda'\lambda''}|^2 \times \{ (n_{\lambda'} + n_{\lambda''} + 1) \delta(\omega_{\lambda} - \omega_{\lambda'} - \omega_{\lambda''}) + (n_{\lambda'} - n_{\lambda''}) [\delta(\omega_{\lambda} + \omega_{\lambda'} - \omega_{\lambda''}) - \delta(\omega_{\lambda} - \omega_{\lambda'} + \omega_{\lambda''})] \}. \quad (1)$$

Here,  $\omega_{\lambda}$  is the harmonic phonon frequency of the phonon mode  $\lambda$ ,  $n_{\lambda} = [\exp(\hbar\omega_{\lambda}/k_B T) - 1]^{-1}$  is the Bose-Einstein distribution at temperature  $T$ , and  $\Phi_{\lambda\lambda'\lambda''}$  denotes the three-phonon-scattering strength.  $\Phi_{\lambda\lambda'\lambda''}$  was obtained by the usual coordinate transformation of third-order force constants from direct space to phonon space.<sup>15</sup> The second- and third-order real-space force constants were obtained by *ab initio* calculation, of which the details are given in the next section.

To more realistically compare the calculated  $\kappa$  with the measured thermal conductivities, the isotopic scattering effect due to the natural isotope distribution was taken into account according to the second-order perturbation theory.<sup>22</sup> Using the relaxation times for the phonon-phonon scattering and isotopic scattering,  $\tau_{\lambda, \text{ph-ph}}$  and  $\tau_{\lambda, \text{iso}}$ , respectively, the total relaxation time for a phonon mode,  $\tau_{\lambda}$ , was calculated by assuming Matthiessen's rule,  $1/\tau_{\lambda} = 1/\tau_{\lambda, \text{ph-ph}} + 1/\tau_{\lambda, \text{iso}}$ .

The experimental thermal conductivities in the Si<sub>3</sub>N<sub>4</sub> system were measured for polycrystalline samples and not from single crystals. The conductivities measured in a polycrystalline area were affected by various lattice defects within that area, such as grain boundaries, impurities, and vacancies. We crudely took them into account by the relaxation time  $\tau_{\lambda, \text{bs}} = L/|\mathbf{v}_{\lambda}|$  of a phonon boundary scattering model, where  $\mathbf{v}_{\lambda} = \nabla_{\mathbf{q}}\omega_{\lambda}$  is the group velocity and  $L$  is a parameter related to the boundary mean free path. We consider  $\tau_{\lambda, \text{bs}}$  as a variable parameter and partly include it in the calculated  $\kappa$ , according to Matthiessen's rule.

The closed form of  $\kappa$  within the RTA was obtained via

$$\kappa = \frac{1}{N_{\mathbf{q}}\Omega} \sum_{\lambda} \tau_{\lambda} \mathbf{v}_{\lambda} \otimes \mathbf{v}_{\lambda} c_{\lambda}, \quad (2)$$

where  $N_{\mathbf{q}}$  is the number of  $\mathbf{q}$ -points,  $\Omega$  is the unit cell volume, and  $c_{\lambda}$  is the mode heat capacity. To analyze  $\kappa$

in detail, the cumulative thermal conductivity:

$$\kappa^c(\omega) = \frac{1}{N_{\mathbf{q}}\Omega} \int_0^\omega \sum_{\lambda} \tau_{\lambda} \mathbf{v}_{\lambda} \otimes \mathbf{v}_{\lambda} c_{\lambda} \delta(\omega' - \omega_{\lambda}) d\omega', \quad (3)$$

and its derivative  $\frac{d\kappa^c(\omega)}{d\omega}$ :

$$\frac{d\kappa^c(\omega)}{d\omega} = \frac{1}{N_{\mathbf{q}}\Omega} \sum_{\lambda} \tau_{\lambda} \mathbf{v}_{\lambda} \otimes \mathbf{v}_{\lambda} c_{\lambda} \delta(\omega - \omega_{\lambda}), \quad (4)$$

were calculated to determine the phonon mode contributions to  $\kappa$ .

## B. Computational details

The force constants required for the lattice dynamics were calculated using the first-principles projector augmented wave method<sup>23</sup> (VASP code<sup>24-26</sup>). The generalized gradient approximation (GGA) parameterized by Perdew, Burke, and Ernzerhof<sup>27</sup> was used for the exchange correlation potential. A plane wave energy cutoff of 500 eV was employed. The crystal structures were optimized for 0 K and 0 GPa until the residual forces acting on the constituent atoms were less than  $10^{-6}$  eV  $\text{\AA}^{-1}$ . Here, the temperature and pressure were considered only for the electronic system and the zero point lattice vibration was not considered. The calculated lattice parameters were  $a = 7.808$   $\text{\AA}$  and  $c = 5.659$   $\text{\AA}$  for the  $\alpha$  phase,  $a = 7.660$   $\text{\AA}$  and  $c = 2.925$   $\text{\AA}$  for the  $\beta$  phase, and  $a = 7.787$   $\text{\AA}$  for the  $\gamma$  phase, which are in agreement with the experimental data<sup>8,9,28</sup> within +0.7 % error. The lattice volume optimized with the local density approximation (LDA)<sup>29</sup> for the exchange correlation potential was, for  $\beta$ - $\text{Si}_3\text{N}_4$ , 3 % smaller than the volume optimized with GGA, which is a typical volume contraction of LDA.  $\kappa_{xx}$  and  $\kappa_{zz}$  calculated with LDA were larger by 0.3 and 2.6 % than those calculated with GGA. For our discussion, these differences are sufficiently small; therefore, the impact of the choice of exchange correlation potential is considered to be minor in this study.

The force constants were calculated by the finite difference approach<sup>30</sup>. For this calculation, the following supercells were adopted:  $1 \times 1 \times 2$ ,  $1 \times 1 \times 3$ , and  $1 \times 1 \times 1$  supercells of the conventional unit cells for the calculations of the third-order force constants of  $\alpha$ ,  $\beta$ , and  $\gamma$ - $\text{Si}_3\text{N}_4$ , respectively, and  $3 \times 3 \times 4$ ,  $3 \times 3 \times 8$  and  $2 \times 2 \times 2$  for those of the second-order force constants. The length of the induced atomic displacements was set to 0.03  $\text{\AA}$ . Table I shows  $\kappa$  calculated with several different sets of the supercells, which indicates that the calculated  $\kappa$  has reasonable convergence with respect to the size of the supercells.

Uniform  $\mathbf{k}$ -point sampling meshes of  $4 \times 4 \times 2$ ,  $4 \times 4 \times 3$ , and  $3 \times 3 \times 3$  were employed for calculations of the third-order force constants of the  $\alpha$ ,  $\beta$ , and  $\gamma$  phases. For the  $\alpha$  and  $\beta$  phases, the center of the  $a^*b^*$  plane was sampled, while the center on the  $c^*$ -axis was not. For

TABLE I. Calculated lattice thermal conductivities of  $\alpha$ -,  $\beta$ -, and  $\gamma$ - $\text{Si}_3\text{N}_4$  ( $\text{W K}^{-1} \text{ m}^{-1}$ ) at 300 K with respect to several combinations of supercell sizes.

Phase	Supercell (# of atoms)		LTC	
	3 <sup>rd</sup> force constants	2 <sup>nd</sup> force constants	$xx$	$zz$
$\alpha$	$1 \times 1 \times 1$ (28)	$1 \times 1 \times 1$ (28)	37	57
	$1 \times 1 \times 2$ (56)	$1 \times 1 \times 2$ (56)	41	79
	$1 \times 1 \times 1$ (28)	$2 \times 2 \times 2$ (224)	55	81
	$1 \times 1 \times 2$ (56)	$2 \times 2 \times 2$ (224)	67	95
	$1 \times 1 \times 2$ (56)	$2 \times 2 \times 3$ (336)	68	97
	$1 \times 1 \times 2$ (56)	$3 \times 3 \times 4$ (1008)	68	100
$\beta$	$1 \times 1 \times 2$ (28)	$1 \times 1 \times 2$ (28)	44	173
	$1 \times 1 \times 2$ (28)	$2 \times 2 \times 4$ (224)	76	208
	$1 \times 1 \times 3$ (42)	$2 \times 2 \times 4$ (224)	71	194
	$1 \times 1 \times 3$ (42)	$2 \times 2 \times 5$ (280)	72	196
	$1 \times 1 \times 3$ (42)	$3 \times 3 \times 8$ (1008)	73	199
$\gamma$	$1 \times 1 \times 1$ (56)	$1 \times 1 \times 1$ (56)	72	
	$1 \times 1 \times 1$ (56)	$2 \times 2 \times 2$ (448)	77	
	$1 \times 1 \times 1$ (56)	$3 \times 3 \times 3$ (56)	79	

the  $\gamma$  phase, a non- $\Gamma$  center mesh was used. For the calculations of the second-order force constants, the  $\Gamma$ -point was only sampled for the  $\alpha$  and  $\beta$  phases, and the only one  $\mathbf{k} = (0.5, 0.5, 0.5)$  point was sampled for the  $\gamma$  phase. The  $\mathbf{q}$ -point sampling meshes of  $10 \times 10 \times 14$ ,  $10 \times 10 \times 26$ , and  $12 \times 12 \times 12$  were employed to calculate  $\kappa$  in Eq. (2) for the  $\alpha$ ,  $\beta$ , and  $\gamma$  phases, respectively.

Non-analytical term correction<sup>31</sup> was applied to the second-order force constants to take into account the long range coulombic forces present in ionic crystals. For the correction, static dielectric constants and Born effective charges were calculated using the density functional perturbation theory as implemented in the VASP code<sup>32,33</sup>.

The effect of lattice thermal expansion on  $\kappa$  was examined by the calculation of  $\kappa$  for several finite temperatures with the crystal structures optimized for the corresponding temperatures within the quasi-harmonic approximation (QHA)<sup>34</sup>. These  $\kappa$  were different from those calculated for the same temperatures with the structure optimized for 0 K. We consider these differences as the effect of lattice thermal expansion. The differences in  $\kappa$  for  $T=300, 600, 900, 1200$ , and,  $1500$  K, for the  $\beta$  phase, were within 1 %. They were similar to those for Si and Ge calculated by Ward *et al.*<sup>35</sup>. For the present study, these differences are negligible and for finite temperatures  $\kappa$  calculated with the structure optimized for 0 K was adopted.

The volumetric thermal expansion coefficients were also calculated. Comparison with the experimental coefficient is useful to validate the present thermal conductivity calculation because both the thermal expansion and  $\kappa$  originate from the anharmonicity of the interatomic potential. The calculated coefficients of the  $\alpha$ ,  $\beta$ , and  $\gamma$  phases were  $4.31 \times 10^{-6}$ ,  $4.19 \times 10^{-6}$ , and  $1.13 \times 10^{-5}$

$\text{K}^{-1}$  for 300 K, while the experimental values<sup>36,37</sup> were  $3.75 \times 10^{-6}$ ,  $3.55 \times 10^{-6}$ , and  $9.48 \times 10^{-6} \text{ K}^{-1}$ . The calculation systematically overestimated the experimental values, but reproduced the experimental tendencies, including that the  $\alpha$  phase has a slightly larger thermal expansion coefficient than the  $\beta$  phase. This supports the validity of the present calculation to qualitatively compare the calculated  $\kappa$  among the  $\text{Si}_3\text{N}_4$  phases.

To compare the microscopic phonon properties among the three phases under the same conditions, the results calculated at 0 GPa are shown and discussed. For the  $\gamma$  phase, this means that we assume the condition of a virtually quenched  $\gamma$  phase at 0 GPa from the high pressure. To examine the analytical continuity of the properties with respect to pressure,  $\kappa$  of the  $\gamma$  phase was calculated at 10, 20, and 40 GPa, as shown in Fig. 8. The phenomenological behavior of the linear dependence of  $\kappa$  with respect to the pressure was reproduced, similar to that in Ref. 38. The slope was  $2.89 \text{ W m}^{-1} \text{ K}^{-1} \text{ GPa}^{-1}$  for the  $\gamma$  phase. From this dependence, we consider that the microscopic values are also varied smoothly with the pressure and those at 0 GPa are valuable for comparison with the corresponding values of the  $\alpha$  and  $\beta$  phases.

### C. Direct solution of LBTE

The advantage of employing the single-mode RTA for thermal conductivity calculations is the closed form, by which the qualitative character of  $\kappa$  can be intuitively understood in terms of the phonon-mode specific properties. The microscopic understanding of the full solution of LBTE is still under development,<sup>39</sup> and the microscopic picture based on collective phonons<sup>40</sup> will require more complicated investigation.

Single-mode RTA solutions of LBTE often underestimate the full solution.<sup>35,41</sup> To check this underestimation,  $\kappa$  for the  $\alpha$  and  $\beta$  phases were calculated by the direct solution of LBTE<sup>21</sup>, which is one of the methods of LBTE full solutions.  $\kappa_{xx}$  and  $\kappa_{zz}$  without the isotope effect were 69 and  $102 \text{ W m}^{-1} \text{ K}^{-1}$  for the  $\alpha$  phase, and 76 and  $238 \text{ W m}^{-1} \text{ K}^{-1}$  for the  $\beta$  phase, respectively, while the corresponding single-mode RTA values were 70 and  $102 \text{ W m}^{-1} \text{ K}^{-1}$  for the  $\alpha$  phase, and 76 and  $210 \text{ W m}^{-1} \text{ K}^{-1}$  for the  $\beta$  phase.  $\kappa_{zz}$  for the  $\beta$  phase from the direct solution was 13 % larger than that of the single-mode RTA solution. The differences in  $\kappa$  between the LBTE solutions are not significant; therefore, we expect that the physics of these lattice thermal conductivities can be well understood within the single-mode RTA at the current level of our interest. Therefore, we discuss the lattice thermal conductivities calculated by the single-mode RTA solution.

## III. RESULTS AND DISCUSSION

### A. Lattice thermal conductivities

TABLE II. Calculated thermal conductivities of  $\alpha$ - $\text{Si}_3\text{N}_4$  (trigonal),  $\beta$ - $\text{Si}_3\text{N}_4$  (trigonal), and  $\gamma$ - $\text{Si}_3\text{N}_4$  (cubic) at 300 K in units of  $\text{W m}^{-1} \text{ K}^{-1}$ , compared with the experimental and theoretical reference data. Theoretical bulk moduli  $B$  (in units of GPa), calculated using the present band method are presented in the fourth column.

	This work			$\kappa$	Ref. Theo.		Ref. Expt.	
	$\kappa_{xx}$	$\kappa_{zz}$	$B$		$\kappa_{xx}$	$\kappa_{zz}$	$\kappa_{xx}$	$\kappa_{zz}$
$\alpha$ - $\text{Si}_3\text{N}_4$	68	100	224	70 <sup>a</sup>	105 <sup>b</sup>	225 <sup>b</sup>	-	-
$\beta$ - $\text{Si}_3\text{N}_4$	73	199	237	250 <sup>a</sup>	170 <sup>b</sup>	450 <sup>b</sup>	69 <sup>c</sup>	180 <sup>c</sup>
$\gamma$ - $\text{Si}_3\text{N}_4$	77	-	296	80 <sup>a</sup>	-	-	-	-

<sup>a</sup> Ref. 19, Slack model.

<sup>b</sup> Ref. 6, molecular dynamics (Green-Kubo).

<sup>c</sup> Ref. 13, single crystalline grains of poly-crystals.

Table II shows the calculated  $\kappa$  for 300 K.  $\beta$ - $\text{Si}_3\text{N}_4$  has a markedly more anisotropic  $\kappa$  than  $\alpha$ - $\text{Si}_3\text{N}_4$ . The directional averages  $\sum_i \kappa_{ii}/3$  are 79, 115, and  $77 \text{ W m}^{-1} \text{ K}^{-1}$  for the  $\alpha$ ,  $\beta$ , and  $\gamma$  phases, respectively. The value for the  $\gamma$  phase is similar to that for the  $\alpha$  phase, despite the comparatively large difference among the bulk moduli ( $B$ ) that are also shown in Table II.

Table II also lists the previously reported experimental<sup>13</sup> and theoretical<sup>6</sup>  $\kappa$  for reference. The theoretical results<sup>19</sup> of the Slack model, which do not include the anisotropy in  $\kappa$ , are shown as  $\kappa$  in Table II. Compared to the  $\kappa$  from MD<sup>6</sup>, our  $\kappa$  for the  $\beta$  phase has better agreement with the experimental  $\kappa$ . Compared to  $\kappa$  from the Slack model, our directional average  $\sum_i \kappa_{ii}/3$  is also much closer to the experimental average.

### B. Dispersion curves [pending!!]

Fig. 2 shows phonon band diagrams for the three  $\text{Si}_3\text{N}_4$  phases. The branches are classified according to their symmetry groups, using different colors and line styles. The solid and dashed lines are used to represent degenerate and non-degenerate modes, respectively. Here we investigate the frequency gradients, the group velocities projected on the paths along the nonequivalent reciprocal axes, with particular focus on their anisotropy in the  $\alpha$  and  $\beta$  phases. This was not investigated in the previous works. The band diagrams on the other high-symmetry paths are almost identical to those reported earlier<sup>18,42</sup> and thus are not shown.

The  $\alpha$  phase unit cell contains two times more basal layer structures than the  $\beta$  phase unit cell; therefore, the edge of the  $\alpha$  phase Brillouin zone in stacking direction  $A$  is half as far as that of the  $\beta$  phase. The number of phonon branches in the  $\alpha$  phase are twice that in the  $\beta$

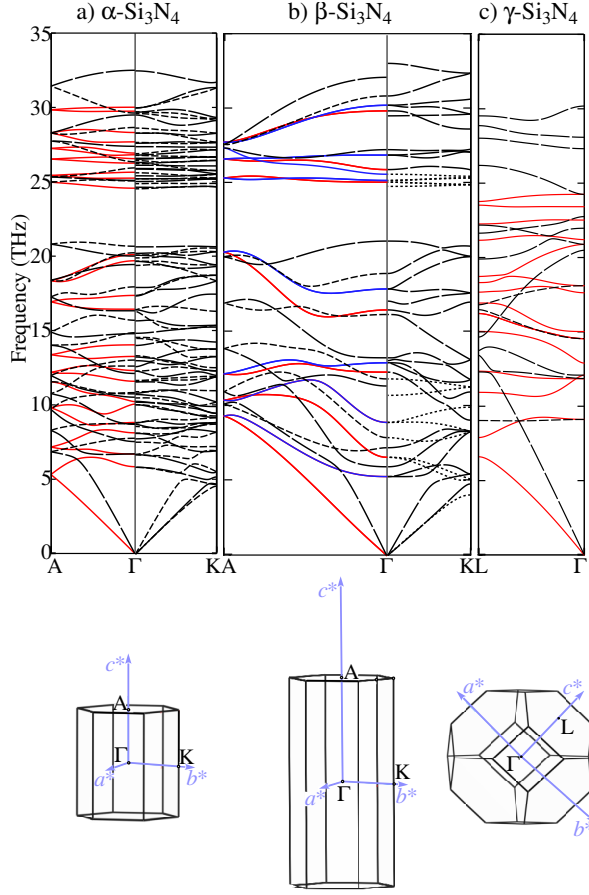


FIG. 2. (color online) Calculated phonon band diagrams (top) for three Si<sub>3</sub>N<sub>4</sub> phases and Brillouin-zones (bottom).

phase. Phonon branches that are adjacent in frequency and belong to the same symmetry group generally show a band gap, and an anticrossing occurs when they are close to each other. If we regard the  $\alpha$  phase lattice as a superlattice of the  $\beta$  phase lattice, then the phonon branches of the  $\alpha$  phase in Fig. 2(a) are produced by folding the phonon branches of the  $\beta$  phase at the perpendicular bisector plane of  $\Gamma A$ . Taking for example the folding of the acoustic phonon branch, in Fig. 2(a), an upper branch that belongs to the same symmetry group is located very close in frequency, which inevitably entails an anticrossing and a band gap between them. This explains why the folded branch, which is degenerate at A with the acoustic branch due to the non-symmorphic symmetry, can not increase its frequency as it goes back on  $\Gamma A$  in Fig. 2(a). The band gap and anticrossings are reported in the theoretical study on the lattice thermal conductivities of GaAs/AlAs superlattices.<sup>43</sup> It is interesting that these effects occur in the present system, due to the stacking manners of the unit structures composed of the same elements.

As a result, in Fig. 2(a), the acoustic phonon branches increase their frequencies similarly between these paths.

In contrast, the corresponding frequencies in Fig. 2(b) increase much more from  $\Gamma$  to A than from  $\Gamma$  to K. The anisotropic frequency increments indicate an anisotropic  $\mathbf{v}_\lambda$ . Compared with the  $\alpha$  and  $\gamma$  phases, the  $\beta$  phase shows significantly steep slopes for the low frequency optical phonon branches on  $\Gamma A$ , which indicates that  $v_{\lambda,z}$  of these phonon modes are large. The anisotropic  $\mathbf{v}_\lambda$  of the acoustic and low-frequency optical phonons will be investigated further in the following sections.

In the  $\gamma$  phase, the longitudinal acoustic branches maintain linear dispersion at higher frequencies than in the other phases. The gradients of  $\omega_\lambda$  for the  $\gamma$  phase are the largest among the three phases, as expected by the largest  $B$ .

### C. $\omega_\lambda$ contour map on the reciprocal plane [add more, for example, isotropic distribution at low frequency i.e., $\lesssim 2$ THz in $\beta$ phase.]

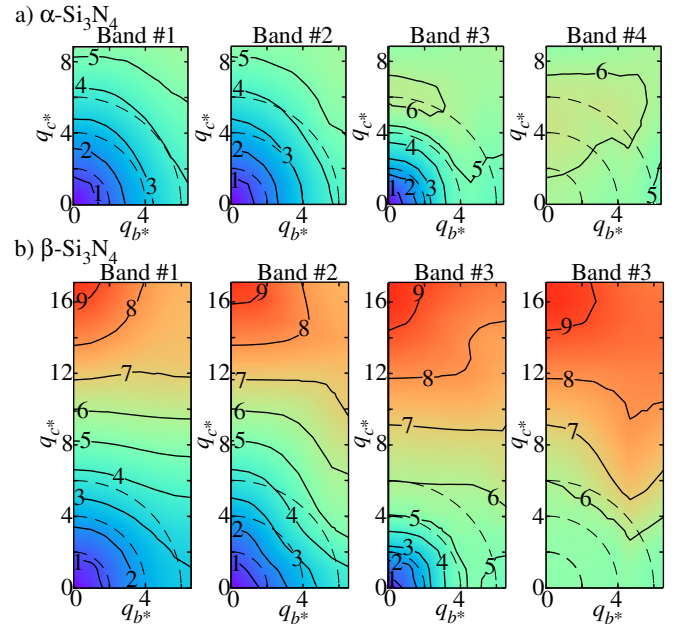


FIG. 3. (color online) Contour maps of phonon frequency (THz) on the  $b^*c^*$  planes of Brillouin-zones. The coordinates in the reciprocal plane are in units of  $10^{-2} \text{ \AA}^{-1}$ . The maps for the four lowest-frequency phonon modes are shown. The frequency landscapes are formed by simply connecting the frequencies of the same band indices, assigned in ascending order of frequency at the respective  $\mathbf{q}$  points.

We investigate the anisotropy in  $\mathbf{v}_\lambda$  of  $\alpha$ - and  $\beta$ -Si<sub>3</sub>N<sub>4</sub> phases using another geometry, i.e., a cross-section of the Brillouin-zone. Fig. 3 shows contour maps of  $\omega_\lambda$  on the  $b^*c^*$  plane. We show the maps for the four lowest-frequency bands because they contribute significantly to  $\kappa$ , which will be confirmed in the next section. There were negligible differences between the distributions on the  $b^*c^*$  plane and the other planes containing the  $c^*$  axis.

Therefore, the  $b^*c^*$  plane was selected as a representative plane. In the  $\alpha$  phase, the  $\omega_\lambda$  distributions and thus  $\mathbf{v}_\lambda$  are almost isotropic. In the  $\beta$  phase, the contours are rather parallel to the  $b^*$  axis, and thus the  $\mathbf{v}_\lambda$  tends to orient toward the  $c^*$  axis direction. This confirms the large anisotropy of  $\mathbf{v}_\lambda$  of the acoustic and low-frequency optical phonon branches for the  $\beta$  phase.

#### D. Frequency distributions of phonon properties

In the previous two sections, we have investigated the anisotropy in  $\mathbf{v}_\lambda$ , which may explain the anisotropy in  $\kappa$ . Here we examine which phonon frequencies and which terms in Eq.(2) characterize the behavior of the present  $\kappa$ . In the following, we disregard the term of mode heat capacity because it is approximately constant for the phonon modes that mainly carry heat at 300 K. For simplicity, the effects of isotope scattering and boundary scattering are not considered. For the investigation, the cumulative thermal conductivity,  $\mathbf{k}^c(\omega)$  in Eq.(4), and its derivative  $d\mathbf{k}^c/d\omega$ , are shown at the top of Fig. 4. From this figure, it is evident that in the  $\alpha$ ,  $\beta$ , and  $\gamma$  phases, the phonon modes with their frequencies up to  $\sim 6$ , 12 and 10 THz largely contribute to each respective  $\kappa$ . The frequencies shown in the contour maps in Fig. 3 are within these frequency ranges, and thus it is confirmed that these bands make a significant contribution to  $\kappa$ .

Assuming that  $\tau_\lambda$  and  $\mathbf{v}_\lambda$  are constant, then  $d\kappa_{ii}^c/d\omega$  ( $ii=xx, zz$ ) are proportional to the phonon DOS:

$$g(\omega) = \frac{1}{N_{\mathbf{q}}\Omega} \sum_{\lambda} \delta(\omega - \omega_{\lambda}). \quad (5)$$

In this context, we view  $g(\omega)$  as frequency distributions of heat carrier density. Alternatively, assuming that only  $\tau_\lambda$  is constant, then  $d\mathbf{k}^c/d\omega$  is proportional to:

$$\mathbf{h}(\omega) = \frac{1}{N_{\mathbf{q}}\Omega} \sum_{\lambda} \mathbf{v}_\lambda \otimes \mathbf{v}_\lambda \delta(\omega - \omega_{\lambda}), \quad (6)$$

from which we examine the impacts of both of  $\mathbf{v}_\lambda$  and the heat carrier density.  $g(\omega)$  and  $\mathbf{h}(\omega)$  are shown in Figs. 4(b) and (c). As for the frequency variation of  $\tau_{\lambda,ph-ph}$ , the phonon linewidths are shown as scatter plots of  $(\Gamma_\lambda, \omega_\lambda)$  in Fig. 4(d).

Comparison of the  $\alpha$  and  $\beta$  phases indicates their linewidth distributions are qualitatively similar, except for a striking difference below  $\sim 5$  THz, which will be examined later. The markedly different  $d\kappa_{ii}^c/d\omega$  between the two phases are therefore ascribed to the corresponding  $h_{ii}$ . The overall spectral shapes of  $g(\omega)$  are also similar between the two phases; therefore,  $\mathbf{v}_\lambda$  alone accounts for the different behavior of  $d\kappa_{ii}^c/d\omega$ . It is thus concluded that the different anisotropy in  $\kappa$  can be qualitatively explained by the different  $\mathbf{v}_\lambda$ , due to the folding effects of the band gaps and anticrossings. In contrast, for the zincblende and wurtzite structures, the group velocities

are suggested to be similar from their band structures<sup>15</sup> because the anticrossings are not created by folding, as the optical branches are located at much higher frequencies than in the present system. This must result in similar  $\kappa$  between these structures, irrespective of the stacking manner.

The  $\gamma$  phase has much different  $g(\omega)$ ,  $\mathbf{h}(\omega)$ , and,  $\Gamma_\lambda$  from the other phases, as expected from the large differences in their crystal structures. The most significant difference is in the phonon linewidths. Below  $\sim 10$  THz, the phonon linewidths are approximately twice as large as those of the other phases. We will examine this in detail later. As a result,  $d\kappa_{xx}^c/d\omega$  has relatively low intensities. The longitudinal acoustic phonon branch increases its frequencies much significantly, as we have examined in the band diagram; therefore,  $d\kappa_{xx}^c/d\omega$  rather gradually attenuates as the frequency increases, occasionally resembling  $d\kappa_{xx}^c/d\omega$  of the  $\beta$  phase.

The similar linewidths between the  $\alpha$  and  $\beta$  phases remains a curiosity, although their group velocities have marked differences. Analogous to the report by Lindsay *et al.*<sup>44</sup>, we can say that  $\Gamma_\lambda$  in the present form is dependent on the phase space for the available two phonons,  $\{\lambda', \lambda''\}$ , and is also dependent on  $|\Phi_{\lambda\lambda'\lambda''}|^2$ . We examine these terms one-by-one. A distribution of two-phonon configurations is represented as a joint DOS (JDOS),  $D_2(\mathbf{q}, \omega)$ :

$$D_2(\mathbf{q}, \omega) = D_2^{(1)}(\mathbf{q}, \omega) + D_2^{(2)}(\mathbf{q}, \omega) \quad (7)$$

where

$$\begin{aligned} D_2^{(1)} &= \frac{1}{N_{\mathbf{q}}Z^2} \sum_{\lambda'\lambda''} \Delta(-\mathbf{q} + \mathbf{q}' + \mathbf{q}'') \\ &\times [\delta(\omega + \omega_{\lambda'} - \omega_{\lambda''}) + \delta(\omega - \omega_{\lambda'} + \omega_{\lambda''})], \\ D_2^{(2)} &= \frac{1}{N_{\mathbf{q}}Z^2} \sum_{\lambda'\lambda''} \Delta(-\mathbf{q} + \mathbf{q}' + \mathbf{q}'') \\ &\times \delta(\omega - \omega_{\lambda'} - \omega_{\lambda''}), \end{aligned}$$

with  $\Delta(\mathbf{x})$  giving 1 if  $\mathbf{x}$  is a reciprocal lattice vector, and otherwise zero.  $Z$  is the number of formula units in the primitive unit cell and is included as a scaling factor to compare JDOS for structures with different  $Z$ . The equation of the linewidth in Eq. (1) contains terms of  $(n_{\lambda'} + n_{\lambda''} + 1)$  and  $(n_{\lambda'} - n_{\lambda''})$ . Thus, in more rigorous study, instead of  $D_2^{(1)}$  and  $D_2^{(2)}$ , we should employ weighted JDOS with these terms. We firstly employ the JDOS in Eq. (7) to intuitively examine the similarity between the linewidths of the  $\alpha$  and  $\beta$  phases. The weighted JDOS (WJDOS) will be briefly shown later, including that of the  $\gamma$  phase.

Fig. 5 shows frequency-functions of JDOS at several different  $\mathbf{q}$ -points. They have very weak  $\mathbf{q}$ -point dependences. In the low frequency region up to  $\simeq 10$  THz,  $D_2^{(1)}$  is dominant between the two terms.  $D_2^{(2)}$  are similar between the phases. In the present  $\text{Si}_3\text{N}_4$  system, the phonon modes of the acoustic and low-frequency optical branches, which largely contribute to  $\kappa$ , are significantly fewer than the other phonon modes. The JDOS



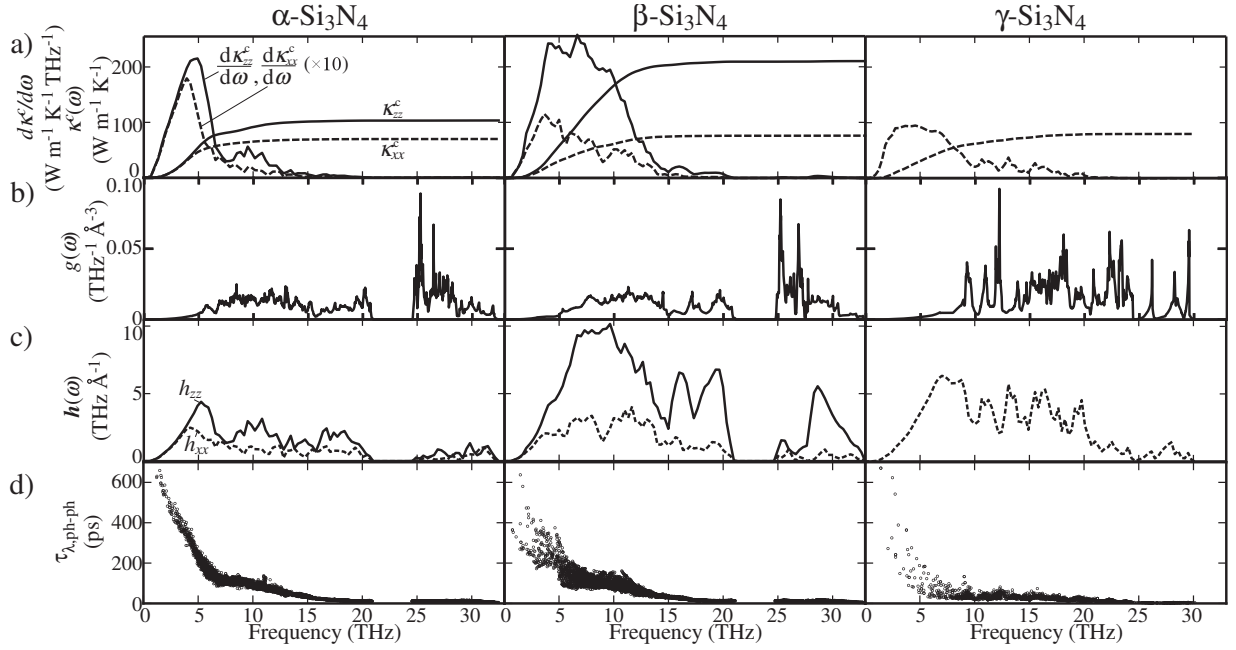


FIG. 4. (color online) Microscopic phonon properties of three  $\text{Si}_3\text{N}_4$  phases. (a) Cumulative thermal conductivity  $\kappa^c$  and its frequency derivative, (b) DOS as  $g(\omega)$ , (c) DOS weighted with  $\mathbf{v}_\lambda \otimes \mathbf{v}_\lambda$  as  $\mathbf{h}(\omega)$ , and (d) scatter plots of phonon lifetimes and phonon frequencies,  $(\tau_\lambda, \omega_\lambda)$ .

are mainly determined by the latter majorities. As in the band diagrams, the branches of the majorities are rather flat. Therefore, in Eq. (7) the dependences of the  $\omega_{\lambda'}$  and  $\omega_{\lambda''}$  on the  $\mathbf{q}'$  and  $\mathbf{q}''$  can be disregarded. In this case,  $D_2^{(1)}$  is simplified to the half part ( $\omega \geq 0$ ) of the auto-correlation function of DOS. The DOSs for both the  $\alpha$  and  $\beta$  phases in Fig. 4(a) have a frequency gap. The  $D_2^{(1)}$  reflect this DOS feature, dropping suddenly around 0 THz with a small shoulder around 5 THz, which corresponds to the width of the gap. The gap originates from the local modes of the planar  $\text{NSi}_3$  that compose each of the  $\alpha$  and  $\beta$  crystal structures;<sup>42</sup> therefore, the  $D_2^{(1)}$  are similar in these phases.

Fig. 6 shows the WJDOS. The terms that corresponds to  $D_2^{(1)}$  and  $D_2^{(2)}$  are denoted as  $N_2^{(1)}$  and  $N_2^{(2)}$ , respectively. They are weighted  $D_2^{(1)}$  and  $D_2^{(2)}$  with  $(n_{\lambda'} - n_{\lambda''})$  and  $(n_{\lambda'} + n_{\lambda''} + 1)$ , respectively. For the comparison among the three phases, we only show the frequency distributions at  $\mathbf{q} = (0, 0, 0)$  because the  $\mathbf{q}$  dependence of the WJDOS was as weak as that for the JDOS. The weighting factors reduce  $N_2^{(1)}$  near 0 THz and enhance  $N_2^{(2)}$  in the high frequency range. The latter reduces  $d\kappa^c/d\omega$  in the high frequency range for all the phases. The total WJDOSs are similar between the  $\alpha$  and  $\beta$  phases. The  $\gamma$  phase has slightly small intensities of the total WJDOS below  $\sim 10$  THz.

As for  $|\Phi_{\lambda\lambda'\lambda''}|^2$ , in Table. III, they are averaged over two frequency ranges of 0–15 or 0–35 THz for  $\omega_\lambda$  and all indices in  $\lambda'$  and  $\lambda''$ . The averages are very similar

TABLE III. Averages of  $|\Phi_{\lambda\lambda'\lambda''}|^2$  over frequency ranges of  $\omega_\lambda$  (0–15 and 0–35 THz) and all  $(\lambda', \lambda')$ . The values are in units of  $10^{-9} \text{ eV}^2 \text{ f.u.}^2$ .

Frequency range (THz)	Phase		
	$\alpha$	$\beta$	$\gamma$
0–15	1.1	1.1	2.3
0–35	5.2	5.2	4.6

for the  $\alpha$  and  $\beta$  phases. With the similar impact of the  $(\text{W})\text{JDOS}$  and  $|\Phi_{\lambda\lambda'\lambda''}|^2$ , the linewidths in these phases are also similar. For the  $\gamma$  phase, the large  $|\Phi_{\lambda\lambda'\lambda''}|^2$  is attributed to the large linewidths. The frequency ranges for  $\omega_\lambda$  were set so that the narrower frequency range approximately corresponds to the range where the phonon modes largely contribute to  $\kappa$ . A small change in the frequency range by a few terahertz did not change the qualitative characteristics of the averages.

Finally, we examine the exceptional, but striking difference in the phonon lifetimes distributions between the  $\alpha$  and  $\beta$  phases. In the  $\alpha$  phase,  $\tau_{\lambda, \text{ph-ph}}$  below  $\sim 5$  THz are aligned on a single smooth line, while in the  $\beta$  phase, they are scattered roughly on two branches. This difference was investigated by an attempt to relate the linewidths to the directions of the atomic vibrations of the phonon modes. Fig. 7 enlarges the  $(\tau_{\lambda, \text{ph-ph}}, \omega_\lambda)$  plots in this frequency range. In Fig. 7(a),  $\tau_{\lambda, \text{ph-ph}}$  are classified using colors according to the sums of the squares of the eigenvector components along the  $\mathbf{q}$ ; the sum is 1

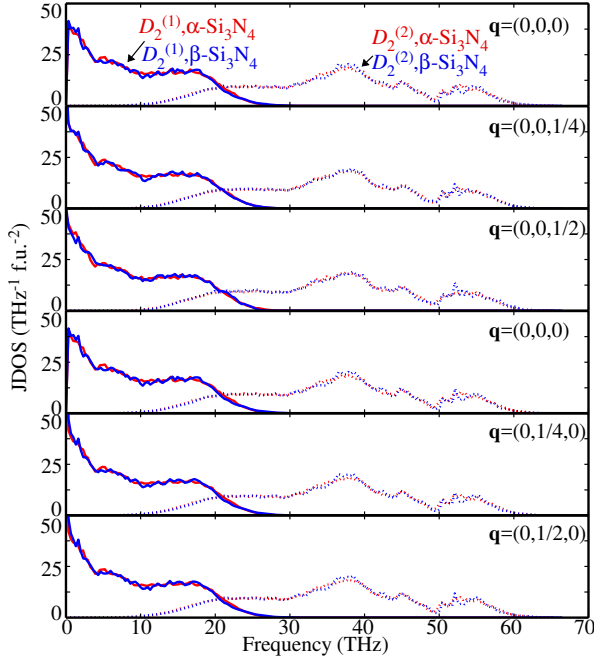


FIG. 5. (color online) JDOS of  $\alpha$ - and  $\beta$ -Si<sub>3</sub>N<sub>4</sub> at different  $\mathbf{q}$  points. The first and fourth rows are JDOS at the same  $\Gamma$ -point but calculated with the polarization for the non-analytic term correction set along  $c^*$  and  $b^*$ , respectively.

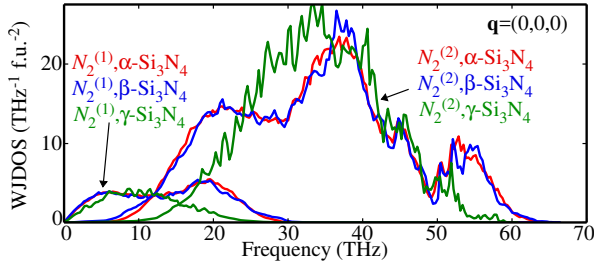


FIG. 6. (color online) Comparison of WJDOS among the three phases at  $\mathbf{q} = (0, 0, 0)$  and 300 K.

for a perfectly longitudinal wave. However, these sums show no clear contrast between the two branches in the  $\beta$  phase. Fig. 7(b) shows the same plot as Fig. 7(a), but with colors according to the sums of the squares of the eigenvector components along the  $ab$  plane, which is 1 when the eigenvector lies in the  $ab$  plane. There is a tendency in the  $\beta$  phase that  $\tau_{\lambda, \text{ph-ph}}$  are short for atomic vibrations along the  $ab$  plane; therefore, the vibration modes along the  $ab$  plane that belong to the acoustic phonon branches are more easily scattered in the  $\beta$  phase, regardless of whether they are longitudinal or transverse. For the panel of  $\beta$ -Si<sub>3</sub>N<sub>4</sub> in Fig. 7(b), a straight line splits the phonon modes into two groups. The numbers of the phonon modes assigned to the smaller and larger  $\Gamma_\lambda$  groups are 145 and 67, of which the ratio is confirmed to be close to the population ratio of the vibration modes along and out of the  $ab$  plane.

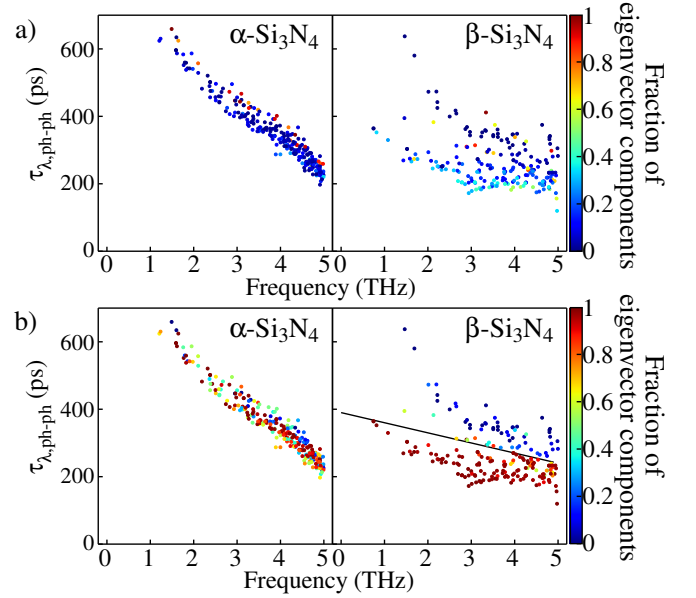


FIG. 7. (color online) Distribution of phonon lifetimes for  $\omega_\lambda \leq 5$  THz shown in color with respect to the strengths of the eigenvector components along (a)  $\mathbf{q}$  and (b) on the  $ab$  plane (b).

#### IV. SUMMARY

In the present study, the lattice thermal conductivities of the three Si<sub>3</sub>N<sub>4</sub> phases were investigated using lattice dynamics based on the first-principles interatomic force constants. The main remarks are as follows:

1) In  $\alpha$ - and  $\beta$ -Si<sub>3</sub>N<sub>4</sub>, of which the crystal structures are characterized by the stacking manner of the basal layer structures,  $\kappa$  is largely altered due to the folding effects of the band gaps and anticrossings. This is in contrast with the zincblende and wurtzite structures in the previous study<sup>15</sup>.  $\kappa$  for  $\alpha$ -Si<sub>3</sub>N<sub>4</sub> is rather isotropic, while  $\kappa_{zz}$  for the  $\beta$  phase is twice or more larger than the other  $\kappa_{ii}$  of the three phases.

2) In the  $\alpha$  phase, the acoustic mode phonons below 6 THz are the main heat carriers, while in the  $\beta$  phase, the phonons below 12 THz contribute to  $\kappa$ . Their group velocities are confirmed to characterize the behavior of  $\kappa$ .

3) In the  $\gamma$  phase, the frequency distribution of the phonon mode contributions to  $\kappa$  is similar to that for  $\kappa_{xx}$  of  $\beta$ -Si<sub>3</sub>N<sub>4</sub>, which is attributed to its large phonon-phonon scattering strength and steep longitudinal acoustic branches.

#### ACKNOWLEDGMENTS

The present work was partly supported by a Grant-in-Aid for Scientific Research (No. 15K14108 from the Ministry of Education, Culture, Sports, Science and Technology (MEXT) Japan and the Elements Strategy Initiative



for Structural Materials (ESISM) of Kyoto University.

### Appendix A: Dependence of the lattice thermal conductivity of $\gamma$ -phase on pressure

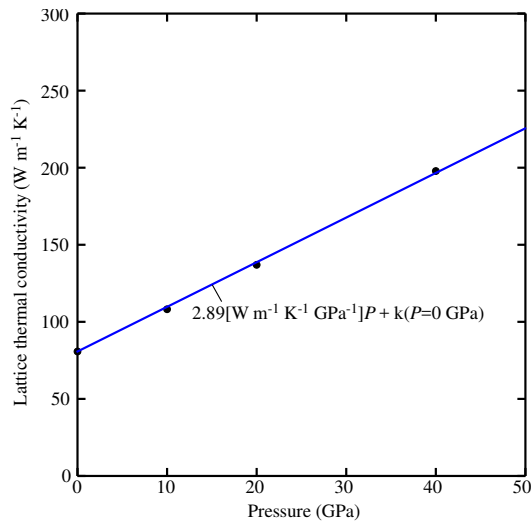


FIG. 8. (color online) Lattice thermal conductivity of  $\gamma$ -Si<sub>3</sub>N<sub>4</sub> as a function of pressure.

\* k-tatsumi@imass.nagoya-u.ac.jp

- <sup>1</sup> G. Slack, Journal of Physics and Chemistry of Solids **34**, 321 (1973).
- <sup>2</sup> Y. Zhou, H. Hyuga, D. Kusano, Y.-i. Yoshizawa, and K. Hirao, Advanced Materials **23**, 4563 (2011).
- <sup>3</sup> K. Hirao, K. Watari, H. Hayashi, and M. Kitayama, MRS Bulletin **26**, 451 (2001).
- <sup>4</sup> K. Watari, Journal of the Ceramic Society of Japan **109**, S7 (2001).
- <sup>5</sup> N. Hirosaki, Y. Okamoto, M. Ando, F. Munakata, and Y. Akimune, Journal of the Ceramic Society of Japan **104**, 49 (1996).
- <sup>6</sup> N. Hirosaki, S. Ogata, C. Kocer, H. Kitagawa, and Y. Nakamura, Physical Review B **65**, 134110 (2002).
- <sup>7</sup> F. L. Riley, Journal of the American Ceramic Society **83**, 245 (2000).
- <sup>8</sup> M. Yashima, Y. Ando, and Y. Tabira, The Journal of Physical Chemistry B **111**, 3609 (2007).
- <sup>9</sup> D. Du Boulay, N. Ishizawa, T. Atake, V. Streltsov, K. Furuya, and F. Munakata, Acta Crystallographica Section B: Structural Science **60**, 388 (2004).
- <sup>10</sup> S. Hampshire, H. Park, D. Thompson, and K. Jack, Nature **274**, 880 (1978).
- <sup>11</sup> T. Hahn, ed., International tables for crystallography, Vol. A (John Wiley & Sons, Inc., 2011).
- <sup>12</sup> T. Hirai, S. Hayashi, and K. Niihara, AM. CERAM. SOC. BULL. Am. Ceram. Soc. Bull. **57**, 1126 (1978).
- <sup>13</sup> B. Li, L. Pottier, J. Roger, D. Fournier, K. Watari, and K. Hirao, Journal of the european ceramic society **19**, 1631 (1999).
- <sup>14</sup> R. Vashishta, R. K. Kalia, A. Nakano, and I. Ebbsö, Amorphous Insulators and Semiconductor, edited by M. F. Thorpe and M. I. Mitkova (Kluwer, 1996).
- <sup>15</sup> A. Togo, L. Chaput, and I. Tanaka, Physical Review B **91**, 094306 (2015).
- <sup>16</sup> A. Zerr, G. Miehe, G. Serghiou, M. Schwarz, E. Kroke, R. Riedel, H. Fueß, P. Kroll, and R. Boehler, Nature **400**, 340 (1999).
- <sup>17</sup> Y. Zhang, A. Navrotsky, and T. Sekine, Journal of materials research **21**, 41 (2006).
- <sup>18</sup> B. Xu, J. Dong, P. F. McMillan, O. Shebanova, and A. Salamat, Physical Review B **84**, 014113 (2011).
- <sup>19</sup> D. Morelli and J. Heremans, Applied physics letters **81**, 5126 (2002).
- <sup>20</sup> A. Togo and I. Tanaka, Scripta Materialia **108**, 1 (2015).
- <sup>21</sup> L. Chaput, Physical review letters **110**, 265506 (2013).
- <sup>22</sup> S.-i. Tamura, Physical Review B **27**, 858 (1983).
- <sup>23</sup> P. E. Blöchl, Phys. Rev. B **50**, 17953 (1994).
- <sup>24</sup> G. Kresse and J. Furthmüller, Physical review B **54**, 11169 (1996).
- <sup>25</sup> G. Kresse, J. Non-Cryst. Solids **193**, 222 (1995).
- <sup>26</sup> D. J. Kresse, Georg, Phys. Rev. B **59**, 1758 (1999).
- <sup>27</sup> J. P. Perdew, K. Burke, and M. Ernzerhof, Phys. Rev. Lett. **77**, 3865 (1996).

- <sup>28</sup> W. Paszkowicz, R. Minikayev, P. Piszora, M. Knapp, C. Bähz, J. Recio, M. Marques, P. Mori-Sánchez, L. Gerward, and J. Jiang, *Phys. Rev. B* **69**, 052103 (2004).
- <sup>29</sup> D. M. Ceperley and B. Alder, *Physical Review Letters* **45**, 566 (1980).
- <sup>30</sup> S. Wei and M. Chou, *Physical review letters* **69**, 2799 (1992).
- <sup>31</sup> Y. Wang, J. Wang, W. Wang, Z. Mei, S. Shang, L. Chen, and Z. Liu, *J. Phys.: Condens. Matter* **22**, 202201 (2010).
- <sup>32</sup> M. Gajdoš, G. Hummer, G. Kresse, J. Furthmüller, and B. F. F., *Phys. Rev. B* **73**, 045112 (2006).
- <sup>33</sup> X. Wu, D. Vanderbilt, and D. R. Hamann, *Phys. Rev. B* **72**, 035105 (2005).
- <sup>34</sup> M. T. Dove, *Introduction to lattice dynamics*, Vol. 4 (Cambridge university press, 1993) pp. 76–77.
- <sup>35</sup> A. Ward and D. Broido, *Physical Review B* **81**, 085205 (2010).
- <sup>36</sup> R. Minikayev, W. Paszkowicz, P. Piszora, M. Knapp, and C. Bähz, “Thermal expansion of and silicon nitride,” (2007).
- <sup>37</sup> W. Paszkowicz and R. Minikayev, *Phys. Rev. B* **69**, 052103 (2004).
- <sup>38</sup> P. Andersson, *Journal of Physics C: Solid State Physics* **18**, 3943 (1985).
- <sup>39</sup> A. Cepellotti and N. Marzari, *Physical Review X* **6**, 041013 (2016).
- <sup>40</sup> R. J. Hardy, *Physical Review B* **2**, 1193 (1970).
- <sup>41</sup> S. Mukhopadhyay, L. Lindsay, and D. J. Singh, *Scientific reports* **6** (2016).
- <sup>42</sup> A. Kuwabara, K. Matsunaga, and I. Tanaka, *Physical Review B* **78**, 064104 (2008).
- <sup>43</sup> W. E. Bies, R. J. Radtke, and E. H. J. Appl. Phys. **88**, 1498 (2000).
- <sup>44</sup> L. Lindsay and D. A. Broido, *J. Phys.: Condens. Matter* **20**, 165209 (2008).